Report

Current Biology

Distinct Mechanisms for Visual and Motor-Related Astrocyte Responses in Mouse Visual Cortex

Highlights

- Astrocytes of moving mice display robust retinotopic responses to visual stimuli
- Sensory responses are distinguishable from responses to locomotion
- Vision-driven responses are correlated to arousal
- Vision- and arousal-driven responses are differentially regulated by noradrenaline

Authors

Michal Slezak, Steffen Kandler, Paul P. Van Veldhoven, Chris Van den Haute, Vincent Bonin, Matthew G. Holt

Correspondence

vincent.bonin@nerf.be (V.B.), matthew.holt@kuleuven.vib.be (M.G.H.)

In Brief

Slezak et al. reveal robust sensory-induced calcium transients in visual cortex astrocytes of locomoting mice. They dissociate spatiotemporal properties of these transients from global events elicited by arousal and demonstrate their differential regulation by noradrenaline.

Slezak et al., 2019, Current Biology 29, 3120–3127
September 23, 2019
https://doi.org/10.1016/j.cub.2019.07.078

CellPress

CellPress

Current Biology
Report

Distinct Mechanisms for Visual and Motor-Related Astrocyte Responses in Mouse Visual Cortex

Michal Slezak,[1,2,10,11] Steffen Kandler,[1,3,10,12] Paul P. Van Veldhoven,[4] Chris Van den Haute,[5,6] Vincent Bonin,[1,3,7,9,*] and Matthew G. Holt[2,8,9,13,*]

[1]Neuro-Electronics Research Flanders (NERF), Kapeldreef 75, 3001 Leuven, Belgium
[2]VIB Center for Brain and Disease Research, Herestraat 49-Box 602, 3000 Leuven, Belgium
[3]IMEC, Kapeldreef 75, 3001 Leuven, Belgium
[4]KU Leuven, Department of Cellular and Molecular Medicine, LIPIT, Herestraat 49-Box 601, 3000 Leuven, Belgium
[5]KU Leuven, Laboratory for Neurobiology and Gene Therapy and Leuven Brain Institute, RK-Herestraat 49-Box 1023, 3000 Leuven, Belgium
[6]KU Leuven, Leuven Viral Vector Core, RK-Herestraat 49, 3000 Leuven, Belgium
[7]KU Leuven, Department of Biology and Leuven Brain Institute, Naamsestraat 59-Box 2465, 3001 Leuven, Belgium
[8]KU Leuven, Department of Neuroscience and Leuven Brain Institute, Herestraat 49-Box 1021, 3000 Leuven, Belgium
[9]Senior author
[10]These authors contributed equally
[11]Present address: BioMed X GmbH, BioMed X Innovation Center, Im Neuenheimer Feld 515, 69120 Heidelberg, Germany
[12]Present address: Biozentrum, University of Basel, Klingelbergstraße 70, 4056 Basel, Switzerland
[13]Lead Contact
*Correspondence: vincent.bonin@nerf.be (V.B.), matthew.holt@kuleuven.vib.be (M.G.H.)
https://doi.org/10.1016/j.cub.2019.07.078

SUMMARY

Astrocytes are a major cell type in the mammalian nervous system, are in close proximity to neurons, and show rich Ca^{2+} activity thought to mediate cellular outputs. Astrocytes show activity linked to sensory [1, 2] and motor [3, 4] events, reflecting local neural activity and brain-wide neuromodulatory inputs. Sensory responses are highly variable [5–10], which may reflect interactions between distinct input types [6, 7, 9]. However, the diversity of inputs generating astrocyte activity, particularly during sensory stimulation and behavior, is not fully understood [11, 12]. Using a combination of Ca^{2+} imaging, a treadmill assay, and visual stimulation, we examined the properties of astrocyte activity in mouse visual cortex associated with motor or sensory events. Consistent with previous work, motor activity activated astrocytes across the cortex with little specificity, reflecting a diffuse neuromodulatory mechanism. In contrast, moving visual stimuli generated specific activity patterns that reflected the stimulus' trajectory within the visual field, precisely as one would predict if astrocytes reported local neural activity. Visual responses depended strongly on behavioral state, with astrocytes showing high amplitude Ca^{2+} transients during locomotion and little activity during stillness. Furthermore, the amplitudes of visual responses were highly correlated with pupil size, suggesting a role of arousal. Interestingly, while depletion of cortical noradrenaline abolished locomotor responses, visual responses were only reduced in amplitude and their spatiotemporal organization remained intact, suggesting two distinct types of inputs underlie visual responses. We conclude that cortical astrocytes integrate local sensory information and behavioral state, suggesting a role in information processing.

RESULTS AND DISCUSSION

To study interactions between sensory and motor activity in cortical astrocytes, we used widefield and cellular Ca^{2+} imaging in primary visual cortex (V1) of head-fixed mice. Animals were habituated to run head-fixed on a treadmill, and the genetically encoded Ca^{2+} indicator GCaMP6m was expressed in V1 astrocytes of the left hemisphere. Ca^{2+} activity of GCaMP-labeled cells was measured using 1-photon and 2-photon imaging, while animals intermittently ran on the treadmill (Figure 1A; STAR Methods). To elicit visual responses, high-contrast checkerboard bar stimuli were moved slowly in one of four cardinal directions across the contralateral, right visual hemifield (Figure 1B; STAR Methods). The visual stimuli moved at speeds of 6°/s interleaved by 10- or 30-s epochs of gray screen and repeated 10 times. Locomotor behavior was encouraged by a water reward. Locomotion and pupil size were continuously monitored.

We first examined, with widefield imaging, the Ca^{2+} responses of V1 astrocytes to locomotion and visual stimulation. To investigate Ca^{2+} responses, we linked the images to locomotion and stimulus onsets and computed the average evoked responses over repeated locomotion events or stimulation trials. Consistent with earlier reports [4, 9], locomotion elicited synchronous activation of astrocytes across the cortex (Figures 1C–1E, S1A,

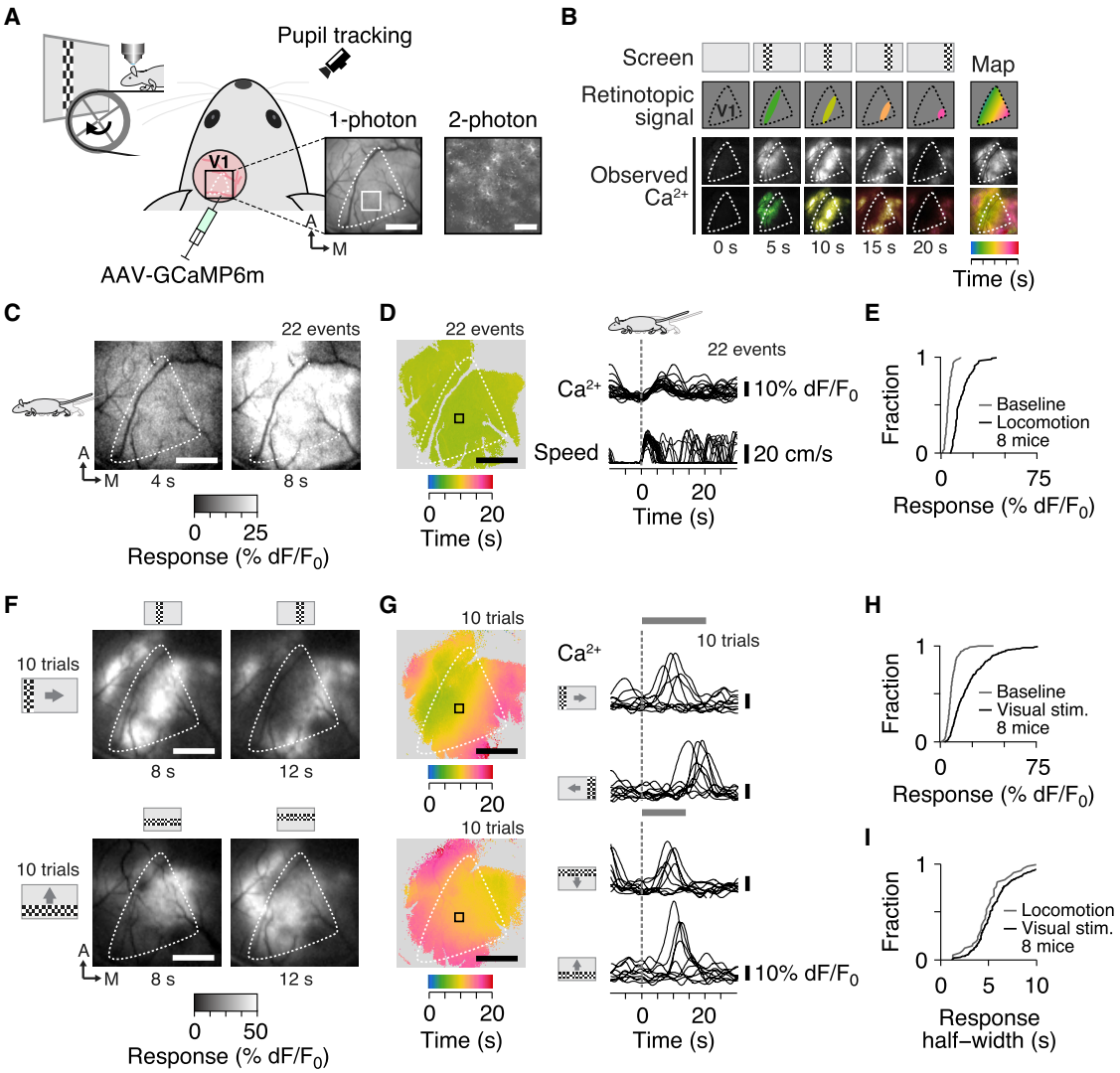

Figure 1. Distinct Ca^{2+} Responses in Astrocytes of the Mouse Visual Cortex during Locomotion and Visual Stimulation

(A) Mice were head-fixed under a dual widefield and multiphoton microscope. To stimulate the right visual field, an LCD monitor was placed in front of the right eye. The right eye was monitored for changes in pupil size. The mice were implanted with a cranial window over the left visual cortex. AAVs encoding the calcium indicator GCaMP6 were delivered by stereotaxic injection. GCaMP6 fluorescence was measured using 1-photon (left) or 2-photon (right) imaging. Anterior (A) and medial (M). Scale bars, 1 mm for 1-photon field of view (FOV), 50 μm for 2-photon FOV.

(B) Visual stimulation paradigm for studying responses of visual cortical astrocytes. Left, top to bottom: time-lapse of checkerboard moving bar stimulus, pseudo-colored schematic of retinotopic response within V1, visually evoked astrocytic Ca^{2+} responses shown in grayscale or pseudo-color coding for time since stimulus onset. Numbers indicate time in seconds. Right, top to bottom: schematic, response maximum intensity projection, and retinotopic map inferred from time to response peak.

(C–E) Voluntary locomotion induces widespread, synchronous activation of astrocytes across the cortex.

(C) Individual black and white frames are 1-s time slices of the event-related averages at indicated times after onset of locomotion. The magnitude of fluorescence increase (% dF/F_0) is shown in grayscale.

(D) Left: pseudo-colored, pixel-wise time to response peak map shows uniform peak response times across the cortex after locomotion onset. Areas of weak GCaMP6 expression (gray) are excluded from analysis (see STAR Methods). Black square indicates ROI for traces to the right. Right: individual GCaMP6 (top) and locomotion speed time traces (bottom) from the same experiment. Dashed line indicates locomotion onset.

(E) Cumulative distribution plot showing peak amplitudes of locomotion-related responses (black, n = 102 events), compared to stationary baseline (gray, n = 105 events). Scale bars, 1 mm. See also Video S1.

(F–H) Mouse visual cortex astrocytes show retinotopically organized responses to moving bars.

(F) Individual black and white frames are 1-s time slices of the stimulus-related averages at indicated times after onset of stimulation.

(G) Left: response maps show time-to-response peak for rightward moving (top) and upward moving (bottom) stimuli. Maps are the average across 10 repeated trials for each direction tested. Right: single-trial GCaMP6 time traces for stimuli moving in each of 4 directions, aligned to the onset of stimuli presentation (dashed lines). Top bars indicate the time at which visual stimulation was present.

(legend continued on next page)

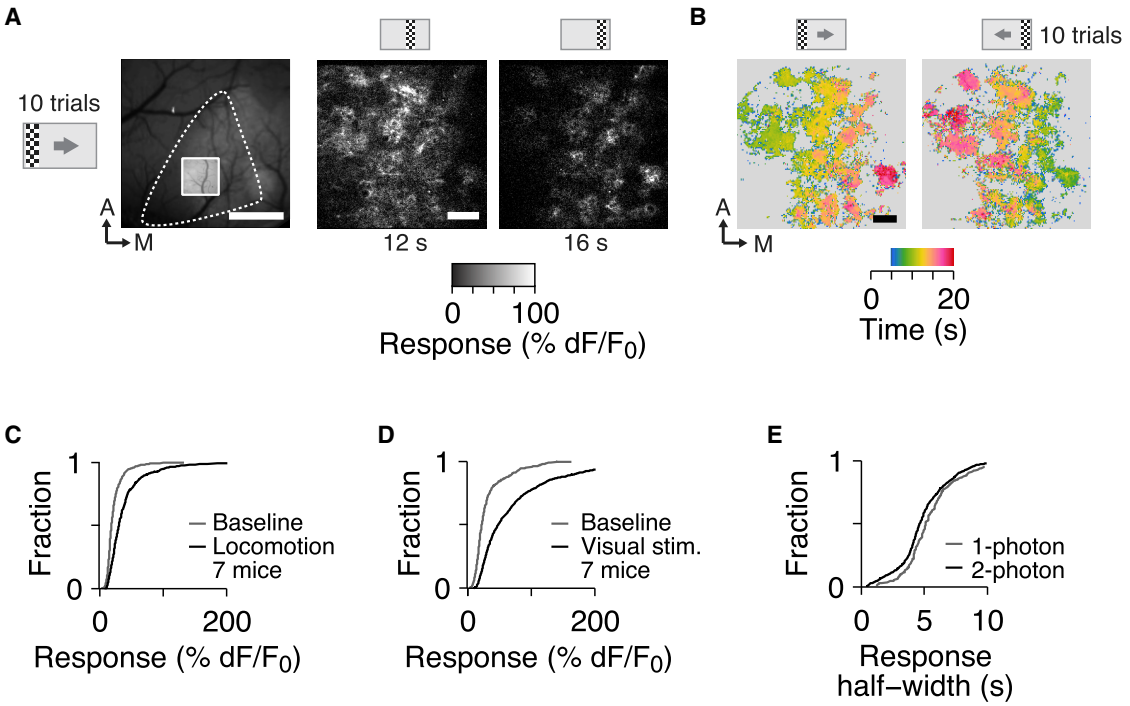

Figure 2. Individual Astrocytes Respond to Visual Stimulation

(A) Left: example 2-photon imaging FOV (white square) at the cortical surface. Dashed line indicates V1. Center and right: 2-photon imaging at 160 μm cortical depth. Black and white frames are 1-s averages obtained at indicated times after visual stimulation onset. Position of the stimulus is indicated above. Scale bars, 1 mm for 1-photon FOV, 50 μm for 2-photon FOV. See also Video S3.

(B) 2-photon response maps showing time-to-response peak relative to visual stimulus onset. Maps are the average of 10 trials for each direction of motion, recorded from a single animal. The pseudo-color scale is adjusted to match the range of delays observed in responses to the moving bar stimuli. Pixels below a fluorescence threshold are shown in gray. Scale bar, 50 μm. See also Video S3.

(C) Cumulative distribution plot showing the amplitudes of locomotion responses (black line, n = 727 events), as compared to activity during preceding stationary epochs (baseline) (gray line, n = 797 events). 7 animals, 133 cells.

(D) Cumulative distribution plots showing the amplitudes of responses to visual stimulation (black line, n = 1,733 trials), as compared to pre-stimulus baseline (gray line, n = 533 events). 7 animals, 133 cells.

(E) Cumulative distribution plots showing the half-width at half-maximum of responses to visual stimulation obtained with 2-photon (black line, n = 1,129 trials, 133 cells, 7 animals) or 1-photon imaging (gray line, n = 233 trials, 8 animals).

See also Figure S1.

and S2A; Video S1). The activation spanned the whole of V1 and surrounding areas. Such unspecific activation is consistent with neuromodulatory inputs that broadly and diffusely innervate the cortex. In contrast, the checkerboard bar stimuli elicited spatially localized activity patterns that moved across the cortex following the bar's trajectory in visual field (Figures 1F–1H and S1B; Video S2). Calculation of time-to-response peak from the data produced smooth maps that reflect V1's topographic organization of visual inputs - retinotopy (Figures 1B, 1G, and S2B; STAR Methods).

To confirm visual and retinotopic responses at the cellular level, we employed 2-photon calcium imaging. Retinotopically organized responses were observed across individual astrocytes (Figures 2A, 2B, and S1C; Video S3), confirming that they did not result from limitations of widefield imaging. Visual responses had consistently larger amplitudes than locomotor responses (Figures 1E versus 1H and 2C versus 2D), suggesting they may reflect a conjunction of inputs. Their time courses, however, were similar (Figures 1I and 2E).

These data demonstrate that astrocytes in mouse visual cortex can respond not only to behavioral state changes but also to local sensory inputs. The dependence of V1 responses on the stimulus' location within the visual field strongly suggests that these responses are generated directly in individual cells, as opposed to passive Ca^{2+} diffusion through the astrocyte network via gap junctions, following triggering of the response [13].

Next, we examined the impact of behavioral state on responses of V1 astrocytes to visual stimulation. Consistent with previous reports [9], strong responses to visual stimuli were observed during locomotor activity, but not during stillness,

(H) Cumulative distribution plots showing peak amplitudes of responses to visual stimulation (black line, n = 438 trials), compared to pre-stimulus baseline (gray line, n = 210 events). Only stationary pre-stimulus windows (8 s) were considered for baseline. Scale bars, 1 mm. See also Video S2.

(I) Cumulative distribution plots showing the half-width at half-maximum of responses to locomotion (gray line, n = 42 events) or visual stimulation (black line, n = 233 trials).

See also Figures S1 and S2.

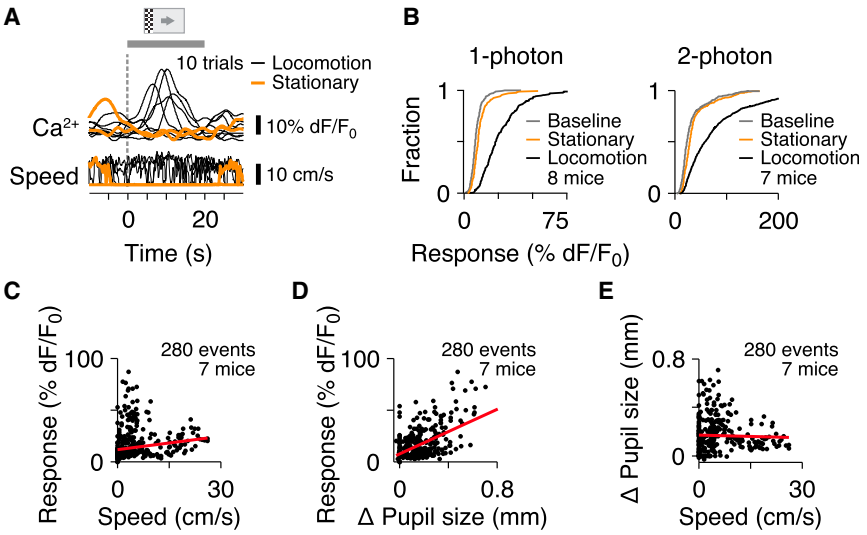

Figure 3. Visual Cortex Astrocytes Integrate Information on Sensory Inputs and Arousal State

(A) Single-trial 1-photon GCaMP6 (top) and movement speed (bottom) traces aligned to stimulus onset (dashed line). Black and orange curves show responses during locomotion and stationarity (no movement from 1 s before visual stimulation onset and during the presentation period), respectively. Bar indicates the time during which visual stimulation was present.

(B) Cumulative distribution plots show peak fluorescence changes upon visual stimulation when the animal is stationary (orange curves) or running (black curves). Data were recorded in 1-photon (left) or 2-photon mode (right). n = 291/1,350 (1-photon/2-photon) trials during running, n = 147/363 trials during stationarity, and n = 210/533 events for pre-stimulation baseline (gray curves).

(C and D) Scatter plots showing the peak fluorescence changes recorded in 1-photon mode during visual stimulation concomitant with voluntary locomotion plotted against the average speed of locomotion (C) or changes in pupil size at onset of stimulation (D).

(E) Changes in pupil size as a function of locomotion speed.

Red lines show results of robust linear regression.

See also Figure S3.

during which Ca^{2+} signals were nearly indistinguishable from baseline (Figures 3A, 3B, and S3). This strong dependence on locomotor state was observed both with widefield imaging and 2-photon imaging of individual astrocytes (Figure 3B, left versus right). Importantly, however, the amplitude of visual responses was only weakly correlated with locomotion speed (Figure 3C; mean Pearson's correlation coefficient [CC] = 0.091, 95% confidence interval [CI] = 0.028–0.158; STAR Methods).

To test for a role of arousal and neuromodulatory inputs in modulating responses to visual stimuli, we investigated the correlation between astrocyte responses and pupil size—because the latter has been previously used as a non-invasive estimate of brain state and neuromodulatory inputs to cortex [14, 15]. Response amplitudes and pupil size changes were highly correlated (Figure 3D; CC = 0.561, CI = 0.469–0.650), whereas correlations between locomotion speed and pupil size changes were comparatively weaker (Figure 3E; CC = −0.063, CI = −0.131–0.004). Thus, local astrocyte responses evoked by visual stimuli are modulated by arousal.

Changes in arousal are linked to the release of the neuromodulator noradrenaline in cortex, from neurons projecting from the locus coeruleus (LC) [16, 17]. Previous reports have suggested that noradrenaline, released upon increased arousal, modulates astrocyte Ca^{2+} responses to visual stimuli [9, 10]. However, the absolute requirement of noradrenaline to elicit sensory responses, and its contribution relative to sensory inputs, remained to be determined. To assess the contribution of noradrenergic inputs to visual responses, we systemically administered DSP-4 to mice [18]. This toxin depletes noradrenaline levels in the CNS, and in previous studies was reported to mimic the effects of acute administration of adrenergic receptor antagonists on locomotion-induced Ca^{2+} transients in astrocytes [7, 9]. In our experiments, DSP-4 reduced noradrenaline content in cortex to ~75% of control (Figure S4A), without overtly affecting mouse behavior (Figures S4B and S4C).

Upon DSP-4 treatment, the correlation between astrocytic Ca^{2+} transients and pupil size was reduced (control versus DSP-4; visual responses, CC = 0.561, CI = 0.469–0.650 versus CC = 0.235, CI = 0.149–0.319, $p \leq 0.001$; locomotion responses, CC = 0.409, CI = 0.233–0.571 versus CC = 0.120, CI = −0.049–0.279, $p \leq 0.001$; mean CC, 95% CI, one-way ANOVA; Figures S4D and S4E), indicating decoupling of astrocyte activity from noradrenergic control. This reduction had distinct impacts on visual and locomotor responses. DSP-4 largely abolished locomotion-induced responses, with astrocytes showing similar Ca^{2+} activity before and after locomotion onset (Figures 4A and 4C). In contrast, visual responses were only mildly affected, showing a reduction in response amplitude but similar temporal dynamics (Figures 4B, 4D, and S4F). Crucially, the spatiotemporal retinotopically organized activity patterns observed in response to visual stimulation remained intact (Figures 4E, 4F, and S4G; Video S4). Thus, sensory responses are modulated by noradrenaline, but they must be driven by another neurotransmitter, in stark contrast to locomotor responses, which depend primarily on noradrenaline inputs.

Taken together, our data indicate that cortical astrocytes can reliably respond to sensory inputs provided the animal is in the aroused state. While previous studies have reported weak vision-induced responses in rodents, the methodologies used prohibited clear evaluation of the relative contributions of sensory- and locomotion-related inputs [5, 10]. Measuring responses to visual stimuli in spontaneously locomoting mice allowed us to distinguish these two types of signals and to demonstrate their synergistic action. Visual responses in astrocytes were strong during locomotion, but almost absent during periods of stillness. Previous studies in head-fixed mice have demonstrated a clear link between locomotion and elevated arousal [15, 19, 20]. Accordingly, astrocyte responses were not only gated by locomotion but response amplitudes were also correlated with changes in pupil size [14, 16, 17]. Consistent

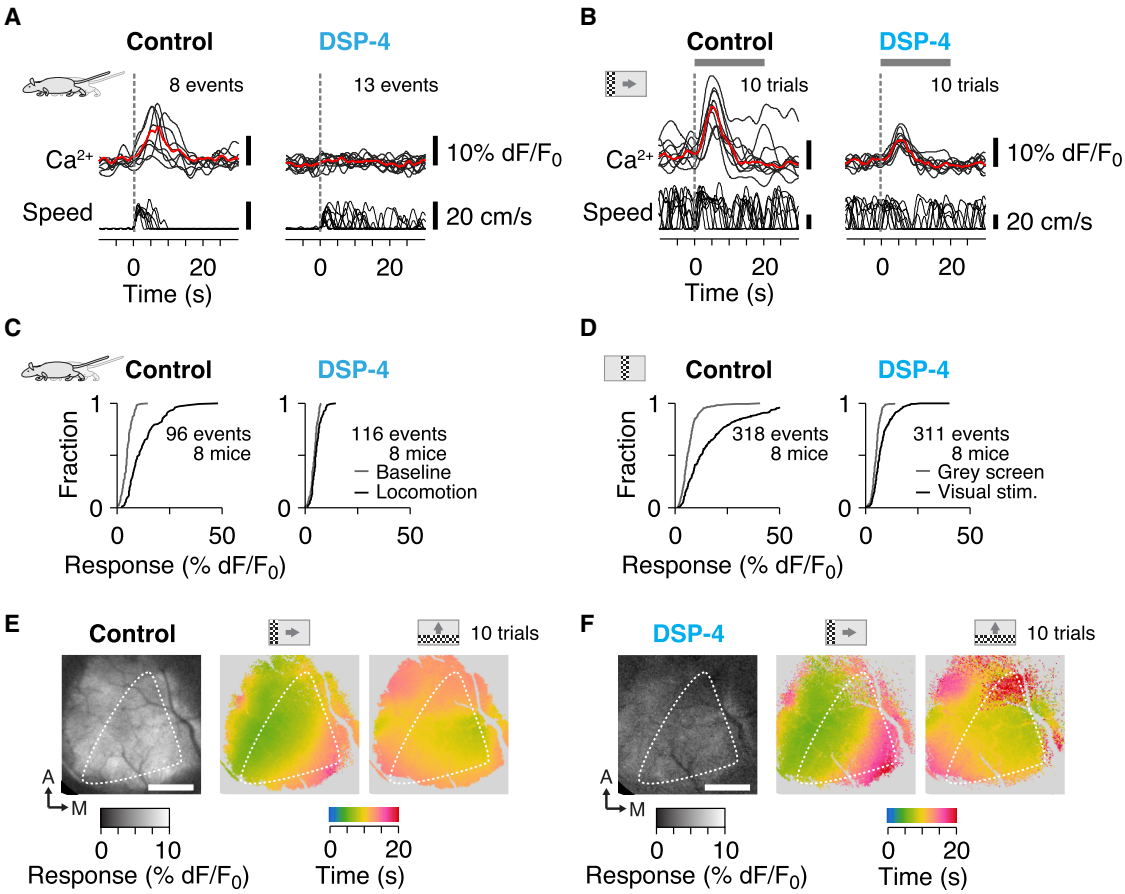

Figure 4. Visually Induced and Locomotion-Related Signals Operate through Distinct Mechanisms

(A) Noradrenaline depletion abolishes the Ca^{2+} responses associated with locomotion onset. Example Ca^{2+} transients (top) recorded using 1-photon imaging from an animal during voluntary locomotion (bottom) pre- (left) and post- (right) DSP-4 administration.

(B) Example Ca^{2+} transients (top) recorded using 1-photon imaging from a mouse during 10 trials of visual stimulation with voluntary locomotion (bottom) pre- (left) and post- (right) DSP-4 administration.

(C) Cumulative distribution plots showing the peak fluorescence during periods of stationarity (no movement for 8 s or more; gray curves) and after locomotion onset (black curves, 8-s window) pre- (left, n = 88 events) and post- (right, n = 114 events) DSP-4 administration. Signal from the strongest responders (90% percentile) after locomotion onset was 11.8% dF/F_0 and 1.3% dF/F_0 above baseline fluorescence before or after DSP-4, respectively.

(D) Cumulative distribution plots show the peak fluorescence before (gray curves) and after (black curves, 8-s window) visual stimulation onset, pre- (left, n = 318 trials) and post- (right, n = 311 trials) DSP-4 administration. Signal from the strongest responders (90% percentile) during visual stimulation was 15.9% dF/F_0 and 4.7% dF/F_0 above pre-stimulation levels before or after DSP-4, respectively. Activity before visual stimulus onset was measured during an 8-s window irrespective of whether the animals were stationary or locomoting. The analysis window was slid independently to be centered approximate to the response peak (STAR Methods).

(E and F) Black and white maps show average activities for vision-induced increases in GCaMP6 fluorescence across trials and stimulus directions. Pseudo-color response maps show the average time to reach maximum GCaMP6 intensity after stimulus onset for the stimulus directions indicated. Maps are the average of 10 trials per stimulus direction in 1 animal pre- (E) and post- (F) DSP-4 administration. Scale bars, 1 mm. See also Figure S4 and Video S4.

with this, DSP-4-mediated depletion of cortical noradrenaline decreased response amplitudes and correlation of responses with pupil size, reinforcing the role of noradrenaline in regulating astrocyte responsiveness to sensory inputs [9].

Our data indicate that astrocyte Ca^{2+} dynamics in rodent cortex are governed by multiple interacting mechanisms. Locomotion-induced responses likely reflect widespread activation of noradrenergic inputs from LC that follow changes in arousal [7, 9]. In contrast, the retinotopically organized visual responses likely reflect local glutamatergic inputs [1, 2]. The retinotopic organization of visual responses indicates that co-incident detection of sensory inputs and behavioral state does not occur at the level of LC neuron firing but likely occurs in the processes of individual V1 astrocytes. In the adult mouse, the astrocyte plasma membrane contains a large repertoire of receptors, including the glutamate receptor mGluR3, as well as α1-, α2-, and β-adrenergic receptors [21–23]. These all belong to distinct classes of G-coupled receptors (G_q, G_i, and G_s). These receptors are organized into microdomains ([24, 25] plus references therein) and inactivate slowly [26], potentially facilitating crosstalk and signal integration [27]. In fact, such a system, involving distinct changes in cyclic AMP (cAMP) and Ca^{2+}, has been demonstrated in cultured astrocytes [28]. This system may serve to fine-tune astrocyte responses according to the sensory and behavioral

inputs involved. Resolving the molecular mechanisms of these respective signaling modalities will require further studies, using a combination of advanced genetic tools and online monitoring systems in freely moving animals [29].

In anesthetized ferrets, synaptic activity elicited by visual stimuli reliably elicited strong local astrocyte responses [1]. In mice, the strongest visually evoked astrocyte responses we observed were dependent on arousal and noradrenaline release. This may reflect technical differences between the studies, including the calcium indicator used and effects of anesthesia. Alternatively, it may reflect the differing organization of the visual cortex between the two species: due to the columnar organization of the cortex in ferret, the majority of neurons within an astrocyte's territory will fire synchronously when presented with a grating stimulus of a particular orientation. In contrast, orientation preference is arranged in a "salt-and-pepper-like" fashion in mouse visual cortex, meaning effective responses will only occur in a fraction of neighboring neurons. Furthermore, firing rates evoked by grating stimuli are nearly three times higher in ferret than in mouse visual cortex [11]. Hence, astrocytes in mouse cortex receive comparatively sparse input, which might require cells to be "primed" in order to detect increased neuronal activity.

In summary, we show that cortical astrocytes integrate signals across input modalities, with behavioral state directly influencing sensory responses. Our data demonstrate the clearest evidence to date for integration of local neurosensory inputs and brain-wide neuromodulatory signals in astrocytes. Such a system is likely to underlie many aspects of astrocyte function regulated by fluctuations in intracellular Ca^{2+}—for example, synaptic plasticity [30–32]. Our data support a role for astrocytes in translating the brain-wide action of neuromodulators to produce specific functional effects on local neuronal circuits [2, 9, 33, 34]. Greater understanding of how such systems operate will undoubtedly further our understanding of coordinated CNS function. It may also help in the design of novel therapies for some of the most devastating neurological conditions, such as Alzheimer's disease, in which loss of noradrenergic transmission, proportional to disease stage, has been observed [35].

STAR★METHODS

Detailed methods are provided in the online version of this paper and include the following:

- KEY RESOURCES TABLE
- LEAD CONTACT AND MATERIALS AVAILABILITY
- EXPERIMENTAL MODEL AND SUBJECT DETAILS
  - Animals
- METHOD DETAILS
  - Surgical procedures and cranial window implantation
  - Mapping of visual areas with flavoprotein imaging
  - Viral vector administration and induction of GCaMP6 expression
  - Treadmill assay and behavioral training
  - 1-photon and 2-photon imaging
  - Visual stimulation
  - Pupil tracking
  - DSP-4 administration and analysis of noradrenaline levels
- QUANTIFICATION AND STATISTICAL ANALYSIS
  - Selection of regions of interest (ROIs)
  - Analysis of calcium activity time courses
  - Calculation of response maps
  - Analysis of locomotion activity
  - Pupil diameter and arousal state
  - Correlation analyses
  - Statistical analyses
- DATA AND CODE AVAILABILITY

SUPPLEMENTAL INFORMATION

Supplemental Information can be found online at https://doi.org/10.1016/j.cub.2019.07.078.

ACKNOWLEDGMENTS

We thank João Couto for providing code for pupil detection; Filip de Vin for technical assistance during experiments; and Ilse Eyckmans, Ingrid Pintens, Eliane Cherretté, and Isabelle Lahousse for administrative assistance. Benjamin Puccio, Molly Kirk, Jessica Mitchell, Daniel Tovbin, Alicja Ronisz, and Frederique Ooms helped with animal training. We thank Dr. Dwight Bergles for advice during the project and Dr. Jérôme Wahis for critical comments on the manuscript. M.G.H. gratefully acknowledges support from the European Research Council (281961), Fonds voor Wetenschappelijk Onderzoek Vlaanderen (FWO) (1523014N and 1527315N), and VIB Institutional Funding. M.S. was supported by a Marie Curie Intra-European Fellowship (331018). V.B. acknowledges support from FWO (G0D0516N), KU Leuven Research Council (C14/16/048), and NERF Institutional Funding. NERF is funded by Imec, VIB, and KU Leuven.

AUTHOR CONTRIBUTIONS

Conceptualization, M.S., S.K., V.B., and M.G.H.; Methodology and Investigation, M.S., S.K., and P.P.V.V.; Resources, C.V.d.H.; Data Analysis and Visualization, M.S., S.K., V.B., and M.G.H.; Writing, M.S., S.K., V.B., and M.G.H.; Funding Acquisition, V.B. and M.G.H.; Supervision, V.B. and M.G.H.

DECLARATION OF INTERESTS

M.S. is an employee at BioMed X GmbH and is funded by Boehringer Ingelheim for work on glial microcircuits and their involvement in psychiatric diseases. The remaining authors have no known conflicts of interest.

Received: January 31, 2019
Revised: June 19, 2019
Accepted: July 26, 2019
Published: September 5, 2019

REFERENCES

1. Schummers, J., Yu, H., and Sur, M. (2008). Tuned responses of astrocytes and their influence on hemodynamic signals in the visual cortex. Science *320*, 1638–1643.
2. Tran, C.H.T., Peringod, G., and Gordon, G.R. (2018). Astrocytes integrate behavioral state and vascular signals during functional hyperemia. Neuron *100*, 1133–1148.
3. Dombeck, D.A., Khabbaz, A.N., Collman, F., Adelman, T.L., and Tank, D.W. (2007). Imaging large-scale neural activity with cellular resolution in awake, mobile mice. Neuron *56*, 43–57.
4. Nimmerjahn, A., Mukamel, E.A., and Schnitzer, M.J. (2009). Motor behavior activates Bergmann glial networks. Neuron *62*, 400–412.
5. Asada, A., Ujita, S., Nakayama, R., Oba, S., Ishii, S., Matsuki, N., and Ikegaya, Y. (2015). Subtle modulation of ongoing calcium dynamics in astrocytic microdomains by sensory inputs. Physiol. Rep. *3*, e12454.

6. Bonder, D.E., and McCarthy, K.D. (2014). Astrocytic G_q-GPCR-linked IP_3R-dependent Ca^{2+} signaling does not mediate neurovascular coupling in mouse visual cortex *in vivo*. J. Neurosci. *34*, 13139–13150.

7. Ding, F., O'Donnell, J., Thrane, A.S., Zeppenfeld, D., Kang, H., Xie, L., Wang, F., and Nedergaard, M. (2013). α1-Adrenergic receptors mediate coordinated Ca^{2+} signaling of cortical astrocytes in awake, behaving mice. Cell Calcium *54*, 387–394.

8. Nizar, K., Uhlirova, H., Tian, P., Saisan, P.A., Cheng, Q., Reznichenko, L., Weldy, K.L., Steed, T.C., Sridhar, V.B., MacDonald, C.L., et al. (2013). *In vivo* stimulus-induced vasodilation occurs without IP_3 receptor activation and may precede astrocytic calcium increase. J. Neurosci. *33*, 8411–8422.

9. Paukert, M., Agarwal, A., Cha, J., Doze, V.A., Kang, J.U., and Bergles, D.E. (2014). Norepinephrine controls astroglial responsiveness to local circuit activity. Neuron *82*, 1263–1270.

10. Sonoda, K., Matsui, T., Bito, H., and Ohki, K. (2018). Astrocytes in the mouse visual cortex reliably respond to visual stimulation. Biochem. Biophys. Res. Commun. *505*, 1216–1222.

11. López-Hidalgo, M., Kellner, V., and Schummers, J. (2017). Astrocyte calcium responses to sensory input: influence of circuit organization and experimental factors. Front. Neural Circuits *11*, 16.

12. Santello, M., Toni, N., and Volterra, A. (2019). Astrocyte function from information processing to cognition and cognitive impairment. Nat. Neurosci. *22*, 154–166.

13. Houades, V., Rouach, N., Ezan, P., Kirchhoff, F., Koulakoff, A., and Giaume, C. (2006). Shapes of astrocyte networks in the juvenile brain. Neuron Glia Biol. *2*, 3–14.

14. Vinck, M., Batista-Brito, R., Knoblich, U., and Cardin, J.A. (2015). Arousal and locomotion make distinct contributions to cortical activity patterns and visual encoding. Neuron *86*, 740–754.

15. McGinley, M.J., Vinck, M., Reimer, J., Batista-Brito, R., Zagha, E., Cadwell, C.R., Tolias, A.S., Cardin, J.A., and McCormick, D.A. (2015). Waking state: rapid variations modulate neural and behavioral responses. Neuron *87*, 1143–1161.

16. Reimer, J., McGinley, M.J., Liu, Y., Rodenkirch, C., Wang, Q., McCormick, D.A., and Tolias, A.S. (2016). Pupil fluctuations track rapid changes in adrenergic and cholinergic activity in cortex. Nat. Commun. *7*, 13289.

17. Breton-Provencher, V., and Sur, M. (2019). Active control of arousal by a locus coeruleus GABAergic circuit. Nat. Neurosci. *22*, 218–228.

18. Jonsson, G., Hallman, H., Ponzio, F., and Ross, S. (1981). DSP4 (N-(2-chloroethyl)-N-ethyl-2-bromobenzylamine)–a useful denervation tool for central and peripheral noradrenaline neurons. Eur. J. Pharmacol. *72*, 173–188.

19. Erisken, S., Vaiceliunaite, A., Jurjut, O., Fiorini, M., Katzner, S., and Busse, L. (2014). Effects of locomotion extend throughout the mouse early visual system. Curr. Biol. *24*, 2899–2907.

20. Aydın, Ç., Couto, J., Giugliano, M., Farrow, K., and Bonin, V. (2018). Locomotion modulates specific functional cell types in the mouse visual thalamus. Nat. Commun. *9*, 4882.

21. Aoki, C. (1992). β-adrenergic receptors: astrocytic localization in the adult visual cortex and their relation to catecholamine axon terminals as revealed by electron microscopic immunocytochemistry. J. Neurosci. *12*, 781–792.

22. Zhang, Y., Chen, K., Sloan, S.A., Bennett, M.L., Scholze, A.R., O'Keeffe, S., Phatnani, H.P., Guarnieri, P., Caneda, C., Ruderisch, N., et al. (2014). An RNA-sequencing transcriptome and splicing database of glia, neurons, and vascular cells of the cerebral cortex. J. Neurosci. *34*, 11929–11947.

23. Zhang, Y., Sloan, S.A., Clarke, L.E., Caneda, C., Plaza, C.A., Blumenthal, P.D., Vogel, H., Steinberg, G.K., Edwards, M.S., Li, G., et al. (2016). Purification and characterization of progenitor and mature human astrocytes reveals transcriptional and functional differences with mouse. Neuron *89*, 37–53.

24. Oheim, M., Schmidt, E., and Hirrlinger, J. (2018). Local energy on demand: are 'spontaneous' astrocytic Ca^{2+}-microdomains the regulatory unit for astrocyte-neuron metabolic cooperation? Brain Res. Bull. *136*, 54–64.

25. Murphy-Royal, C., Dupuis, J.P., Varela, J.A., Panatier, A., Pinson, B., Baufreton, J., Groc, L., and Oliet, S.H. (2015). Surface diffusion of astrocytic glutamate transporters shapes synaptic transmission. Nat. Neurosci. *18*, 219–226.

26. Lohse, M.J., Hoffmann, C., Nikolaev, V.O., Vilardaga, J.P., and Bünemann, M. (2007). Kinetic analysis of G protein-coupled receptor signaling using fluorescence resonance energy transfer in living cells. Adv. Protein Chem. *74*, 167–188.

27. Ryzhov, S., Goldstein, A.E., Biaggioni, I., and Feoktistov, I. (2006). Cross-talk between G_s- and G_q-coupled pathways in regulation of interleukin-4 by A_{2B} adenosine receptors in human mast cells. Mol. Pharmacol. *70*, 727–735.

28. Horvat, A., Zorec, R., and Vardjan, N. (2016). Adrenergic stimulation of single rat astrocytes results in distinct temporal changes in intracellular Ca^{2+} and cAMP-dependent PKA responses. Cell Calcium *59*, 156–163.

29. Scott, B.B., Thiberge, S.Y., Guo, C., Tervo, D.G.R., Brody, C.D., Karpova, A.Y., and Tank, D.W. (2018). Imaging cortical dynamics in GCaMP transgenic rats with a head-mounted widefield macroscope. Neuron *100*, 1045–1058.

30. Chen, N., Sugihara, H., Sharma, J., Perea, G., Petravicz, J., Le, C., and Sur, M. (2012). Nucleus basalis-enabled stimulus-specific plasticity in the visual cortex is mediated by astrocytes. Proc. Natl. Acad. Sci. USA *109*, E2832–E2841.

31. Monai, H., Ohkura, M., Tanaka, M., Oe, Y., Konno, A., Hirai, H., Mikoshiba, K., Itohara, S., Nakai, J., Iwai, Y., and Hirase, H. (2016). Calcium imaging reveals glial involvement in transcranial direct current stimulation-induced plasticity in mouse brain. Nat. Commun. *7*, 11100.

32. Nagai, J., Rajbhandari, A.K., Gangwani, M.R., Hachisuka, A., Coppola, G., Masmanidis, S.C., Fanselow, M.S., and Khakh, B.S. (2019). Hyperactivity with disrupted attention by activation of an astrocyte synaptogenic cue. Cell *177*, 1280–1292.

33. Bazargani, N., and Attwell, D. (2017). Amines, astrocytes, and arousal. Neuron *94*, 228–231.

34. Ma, Z., Stork, T., Bergles, D.E., and Freeman, M.R. (2016). Neuromodulators signal through astrocytes to alter neural circuit activity and behaviour. Nature *539*, 428–432.

35. Leanza, G., Gulino, R., and Zorec, R. (2018). Noradrenergic hypothesis linking neurodegeneration-based cognitive decline and astroglia. Front. Mol. Neurosci. *11*, 254.

36. Chen, T.W., Wardill, T.J., Sun, Y., Pulver, S.R., Renninger, S.L., Baohan, A., Schreiter, E.R., Kerr, R.A., Orger, M.B., Jayaraman, V., et al. (2013). Ultrasensitive fluorescent proteins for imaging neuronal activity. Nature *499*, 295–300.

37. Liu, B., Paton, J.F., and Kasparov, S. (2008). Viral vectors based on bidirectional cell-specific mammalian promoters and transcriptional amplification strategy for use *in vitro* and *in vivo*. BMC Biotechnol. *8*, 49.

38. Roy, M.O., Leventis, R., and Silvius, J.R. (2000). Mutational and biochemical analysis of plasma membrane targeting mediated by the farnesylated, polybasic carboxy terminus of K-ras4B. Biochemistry *39*, 8298–8307.

39. Young, K.M., Mitsumori, T., Pringle, N., Grist, M., Kessaris, N., and Richardson, W.D. (2010). An *Fgfr3-iCreER*^{T2} transgenic mouse line for studies of neural stem cells and astrocytes. Glia *58*, 943–953.

40. Schneider, C.A., Rasband, W.S., and Eliceiri, K.W. (2012). NIH Image to ImageJ: 25 years of image analysis. Nat. Methods *9*, 671–675.

41. Thévenaz, P., Ruttimann, U.E., and Unser, M. (1998). A pyramid approach to subpixel registration based on intensity. IEEE Trans. Image Process. *7*, 27–41.

42. Goldey, G.J., Roumis, D.K., Glickfeld, L.L., Kerlin, A.M., Reid, R.C., Bonin, V., Schafer, D.P., and Andermann, M.L. (2014). Removable cranial windows for long-term imaging in awake mice. Nat. Protoc. *9*, 2515–2538.

43. Schuett, S., Bonhoeffer, T., and Hübener, M. (2002). Mapping retinotopic structure in mouse visual cortex with optical imaging. J. Neurosci. *22*, 6549–6559.

44. Tohmi, M., Takahashi, K., Kubota, Y., Hishida, R., and Shibuki, K. (2009). Transcranial flavoprotein fluorescence imaging of mouse cortical activity and plasticity. J. Neurochem. *109* (*Suppl 1*), 3–9.

45. Rincon, M.Y., de Vin, F., Duqué, S.I., Fripont, S., Castaldo, S.A., Bouhuijzen-Wenger, J., and Holt, M.G. (2018). Widespread transduction of astrocytes and neurons in the mouse central nervous system after systemic delivery of a self-complementary AAV-PHP.B vector. Gene Ther. *25*, 83–92.

46. Fripont, S., Marneffe, C., Marino, M., Rincon, M.Y., and Holt, M.G. (2019). Production, purification, and quality control for adeno-associated virus-based vectors. J. Vis. Exp. *143*, e58960.

47. Slezak, M., Göritz, C., Niemiec, A., Frisén, J., Chambon, P., Metzger, D., and Pfrieger, F.W. (2007). Transgenic mice for conditional gene manipulation in astroglial cells. Glia *55*, 1565–1576.

48. Mao, D., Kandler, S., McNaughton, B.L., and Bonin, V. (2017). Sparse orthogonal population representation of spatial context in the retrosplenial cortex. Nat. Commun. *8*, 243.

49. Royer, S., Zemelman, B.V., Losonczy, A., Kim, J., Chance, F., Magee, J.C., and Buzsáki, G. (2012). Control of timing, rate and bursts of hippocampal place cells by dendritic and somatic inhibition. Nat. Neurosci. *15*, 769–775.

50. Thorré, K., Pravda, M., Sarre, S., Ebinger, G., and Michotte, Y. (1997). New antioxidant mixture for long term stability of serotonin, dopamine and their metabolites in automated microbore liquid chromatography with dual electrochemical detection. J. Chromatogr. B Biomed. Sci. Appl. *694*, 297–303.

51. De Benedetto, G.E., Fico, D., Pennetta, A., Malitesta, C., Nicolardi, G., Lofrumento, D.D., De Nuccio, F., and La Pesa, V. (2014). A rapid and simple method for the determination of 3,4-dihydroxyphenylacetic acid, norepinephrine, dopamine, and serotonin in mouse brain homogenate by HPLC with fluorimetric detection. J. Pharm. Biomed. Anal. *98*, 266–270.

52. Kovesi, P. (2015). Good colour maps: how to design them. arXiv, arXiv:1509.03700.

STAR★METHODS

KEY RESOURCES TABLE

REAGENT or RESOURCE	SOURCE	IDENTIFIER
Bacterial and Virus Strains		
AAV5.CAG.Flex.GCaMP6m.WPRE.SV40	Penn Vector Core	AV-5-PV2817
AAV5.gfaABC1D.Kmyr.GCaMP6m	GCaMP6m [36]	Addgene #40754
	gfaABC1D [37]	Addgene #19976
	Kmyr tag [38]	N/A
Chemicals, Peptides, and Recombinant Proteins		
Alexa Fluor-568	Invitrogen	Cat# A20003
Kerr Tab 2000 dental cement and liquid	Kerr Dental	Cat# 61770
Metabond dental cement	Crown & Bridge	Cat# S380
N-(2-chloroethyl)-N-ethyl-2-bromobenzylamine hydrochloride (DSP-4)	Sigma Aldrich	Cat# C8417
Noradrenaline	Sigma Aldrich	Cat# A7257
Optical glue	Norland	Cat# NOA71
Tamoxifen	Sigma Aldrich	Cat# T5648
Vetbond	3M	Cat# 1469SB
Experimental Models: Organisms/Strains		
Mouse: B6;CBA-Tg(Fgfr3-icre/ERT2)4-2Wdr/J	Univ. College London [39]	RRID: IMSR_JAX:025809
Oligonucleotides		
iCre250 (GAG GGA CTA CCT CCT GTA CC)	[39]	N/A
iCre880 (TGC CCA GAG TCA TCC TTG GC)	[39]	N/A
Software and Algorithms		
Adobe Illustrator	Adobe	RRID: SCR_010279
Breeze 3.20	Waters	https://www.waters.com/waters/de_DE/Breeze-2-HPLC
ImageJ	[40]	RRID: SCR_003070
MATLAB	MathWorks	RRID: SCR_001622
Presentation	Neurobehavioral Systems	RRID: SCR_002521
StreamPix	Norpix	RRID: SCR_015773
TurboReg	[41]	RRID: SCR_014308
Other		
Blackout material	Thorlabs	BK5
Camera: CCD camera	Allied Vision	Prosilica GC660
Camera: EMCCD camera	Qimaging	EM-C^2
Collimating lens	Thorlabs	N-BK7
Cover glasses	Harvard Apparatus	CS-5R, CS-8R
GaAsP photomultipler tubes	Hamamatsu	H11706-401
Galvanometer scanner	Cambridge Technology	6215H
Filters	Semrock	FF01-510/84-25-STR
Laser	Spectra Physics	MaiTai DeepSee
LCD monitor	Samsung	2233RZ
LEDs	Thorlabs	MCWHL5
LED driver	Thorlabs	LEDD1B
Lens	Navitar	Zoom 6000
Lens: 2x widefield lens, NA = 0.55	Edmund Optics	PSM-PLAPO2xPA
Lens: 16x lens, NA = 0.8	Nikon	N16XLWD-PF
Microcontroller	Atmel	AT89LP52

(*Continued on next page*)

Continued

REAGENT or RESOURCE	SOURCE	IDENTIFIER
Multi-wavelength fluorescence detector	Waters	2475
Nanoliter injector: Nanoject II	Drummond Sci.	3-000-205A
Neoprene O-rings 014-018	WPI	016-5927-100; 015-5927-100
Photodetector	Omron	E3T-SR41
Pinch valve	msscientific	075P2NC12-02SQM
Resonant scanner	Cambridge Technology	CRS 8k
Reversed phase column	Alltima	HP C18 AQ
Rotary encoder	Avago Tech	630-HEDS-5540-C02
Stereoscope	Zeiss	MZ10F
Thermistor	CWE Inc	YSI-451
Titanium head plate	Inhouse	Design available upon request
Treadmill	Inhouse / Thorlabs	Design available upon request
Treadmill belt: Velcro material	Country Brook	L-BLA-2
Treadmill belt: Velvet material	McMaster-Carr	88015K1
2-photon microsope	Neurolabware	N/A
Ultrasonic processor	Hielscher	UP50H
USB acquisition board	MCC	USB-4301
USB programmer	Mouser	932-MIKROE-29

LEAD CONTACT AND MATERIALS AVAILABILITY

Further information and requests for resources and reagents should be directed to and will be fulfilled by the Lead Contact, Matthew Holt (Matthew.Holt@kuleuven.vib.be). Viral vectors generated in this study are available from Matthew Holt.

EXPERIMENTAL MODEL AND SUBJECT DETAILS

Animals

All procedures were performed in compliance with protocols approved by the Animal Ethics Committee of the University of Leuven (KU Leuven, Belgium). Experiments involved 15 male *Fgfr3-iCreER^{T2}* hemizygous mice and 3 wild-type (WT) mice bred on a C57BL/6j background (Charles River). *Fgfr3-iCreER^{T2}* mice expressed tamoxifen-inducible Cre recombinase specifically in astrocytes [39]. Genotyping was performed by PCR using primers iCre250 (5′-GAGGGACTACCTCCTGTACC-3′) and iCre880 (5′-TGCCCAGAGT CATCCTTGGC-3′). Animals were group-housed (up to five mice per cage) under standard conditions, under a 12-h:12-h light:dark cycle, with access to food and water *ad libitum* and only moved to individual housing after surgery.

Animals were eight weeks of age or older at the time of headpost and cranial window implantation. Animals were habituated to head fixation and treadmill running (2 - 4 weeks). Their visual cortex was mapped with widefield flavoprotein imaging and injected with AAV. For *Fgfr3-iCreER^{T2}* mice, injections were immediately followed by tamoxifen treatment. Multiple 1-photon and 2-photon imaging experiments were performed for up to 20 weeks after AAV injections. In a subset of animals (N = 10 *Fgfr3-iCreER^{T2}* and 3 WT), imaging sessions were interrupted by a single dose of DSP-4 or saline (as a control). Imaging sessions resumed 72 hours after drug administration. Behavioral training was maintained throughout the experiments. At the end of a given set of experiments, animals were euthanized. For animals injected with DSP-4 (or saline), brains were removed for HPLC analysis.

METHOD DETAILS

Surgical procedures and cranial window implantation

All surgical procedures were performed in aseptic conditions under isoflurane anesthesia (induction 2.5%, 1 l/min O_2; maintenance 1%–1.5%, 0.6 l/min O_2) using a stereotaxic apparatus, a heating pad set to 37°C, and regular toe pinches to assess depth of anesthesia. Animals were treated with dexamethasone (8 mg/kg, intramuscular) four hours prior to surgery to prevent brain swelling. A custom-made titanium head plate and a removable cranial window were implanted to allow head fixation and provide optical access to the left posterior cortex [42]. The scalp was disinfected (70% ethanol and betadine), the skull was exposed, and the temporalis muscle was separated. The head plate was positioned over the posterior left hemisphere and attached using cyanoacrylic glue (Loctite, Henkel). Any exposed tissue or skull was covered with cyanoacrylic glue (Vetbond, 3M) and the head plate was cemented with Metabond (C&B). A 5 mm craniotomy centered over left primary visual cortex (1.6 mm anterior from lambda, 3.1 mm lateral from midline) was covered with a cranial window consisting of one 8 mm and two 5 mm circular coverslips glued concentrically together

with optical glue (NOA71, Norland), and attached to the skull with dental cement (Kerr Tab 2000, KemDent). The implant was painted with a mixture of dental cement and black pigment to prevent stray light from reaching the objective. A water well made of two neoprene O-rings was attached to the head plate using cyanoacrylic glue. After surgery, mice were moved to individual housing and allowed to recover. All mice received post-operative treatment for 60 hours to minimize pain and prevent infection. Buprenorphine (0.2 mg/kg) and cefazolin (15 mg/kg) were supplied via intramuscular injection at 12-hour intervals for 2.5 consecutive days. Trimethoprim (0.1 mg/ml) and sulfamethoxazole (0.5 mg/ml) were supplied in the drinking water for a maximum of 10 days post-surgery.

Mapping of visual areas with flavoprotein imaging

To target viral vector injections, retinotopic mapping of visual areas was performed with flavoprotein imaging [43, 44] during responses to square-wave moving stimuli (spatial frequency = 0.08 cycles per degree, temporal frequency = 4 Hz, horizontal and vertical orientations moving in four cardinal directions) presented at six screen locations (in a 2-by-3 matrix from upper-central to bottom-peripheral right visual hemifield). Each of the six stimuli filled a circular spot covering 40 degrees in visual space along both the horizontal and vertical axes and lasted 8 s. Stimuli were interleaved by equally-timed 'blanks' (50% luminance), with a final 'blank' phase of 8-s duration. This cycle was repeated 10 times. Fractional changes in fluorescence were normalized to baseline and averaged across 4-s intervals to capture the slow time course of the flavoprotein signal. The location of V1 was identified based on the characteristic decrease in flavoprotein fluorescence (relative to the pre-stimulus baseline) observed during presentation of visual stimuli, which distinguishes V1 from surrounding higher visual areas.

Viral vector administration and induction of GCaMP6 expression

Two vector systems were used to deliver GCaMP6m [36] to the visual cortex. Wild-type animals were injected with an AAV-based vector carrying membrane-tagged GCaMP under the control of an astrocyte-specific promoter (AAV5-gfaABC1D-Kmyr-GCaMP6m). AAV was produced *in house*, using a standard tri-transfection protocol with subsequent iodixanol-based purification. Vector titer was determined by quantitative PCR and purity assessed by SDS-PAGE and silver staining [45, 46]. When using the *Fgfr3-iCreER*^{T2} line, animals received injections of AAV5-CAG-Flex-GCaMP6m, which was obtained from the University of Pennsylvania Vector Core. GCaMP6 expression was induced by administration of tamoxifen (see below).

Three to four vector injections were performed along the border of V1 (based on flavoprotein imaging) to cover a large fraction of primary visual cortex. The cranial window was removed with a surgical drill. A microliter injection system (Nanoject II, Drummond Science) was used to inject 100 - 300 nl of a vector containing solution (approximately 9×10^5 to 3×10^6 total vector genomes), together with the fluorescent dye Alexa-568. We typically targeted astrocytes in cortical layer II/III, approximately 120 - 300 μm below the cortical surface. The solution was delivered through beveled glass capillaries (Drummond Science) with 20 - 40 μm tip diameters, at a rate of 60 nl/min. A fluorescence microscope was used to monitor the injections. A new cranial window was fixed in place and the animal was left to recover for five days. When necessary, Cre activation (leading to GCaMP6m expression) was induced by intraperitoneal injection of tamoxifen (2 mg in a mixture of 1 part ethanol - 9 parts sunflower oil; total injection volume 100 μl; Sigma). Tamoxifen administration started immediately after AAV injections and was performed daily for five consecutive days [47], prior to the start of imaging experiments.

Treadmill assay and behavioral training

The treadmill apparatus consisted of a 150 cm long, 5 cm wide belt of Velcro (Country Brook), mounted on two 10 cm diameter wheels, supported by a custom frame (Thorlabs) [48, 49]. Treadmill rotation, and the distance traveled by the animal, was monitored with a resolution of 3.14 mm by a rotary encoder (Avago Tech), attached to the treadmill shaft. Completion of a full lap (150 cm) was recorded using a reflective strip attached to the underside of the belt, which was detected by a photoelectric sensor (Omron). This event triggered the opening of an electromagnetic pinch valve (msscientific), leading to delivery of a drop of tap water, or 10% sucrose solution, through a spout that was accessible to the animal. Recordings of treadmill rotation and lap completion were collected by a custom circuit board with a microcontroller (AT89LP52, Atmel), which linked treadmill position to valve opening. All signals were acquired by a personal computer via a USB data acquisition board (MCC), sampled at 10 kHz and recorded with Presentation software (Neurobehavioral Systems).

Five days after cranial window implantation, mice were put on a water restriction schedule (5 min/day of unrestricted access to water), which was maintained throughout behavioral training and imaging experiments. Mice were manually handled in daily sessions for 3 - 5 days before surgical procedures and, after 5 days of recovery, trained to run head-fixed on a treadmill apparatus for a water reward. The duration of training sessions increased gradually from a few minutes per day up to 1 hour per day, over a period of 2 - 3 weeks. Training was completed when animals reached the desired level of locomotor activity – typically 3 laps of the treadmill per minute. Animal training continued during the experimental phase, with at least two sessions per week, on days when experiments were not being performed.

1-photon and 2-photon imaging

All imaging was conducted using a dual widefield and 2-photon *in vivo* microscope (Neurolabware). Widefield flavoprotein and calcium imaging were performed with blue excitation light (470 nm, Thorlabs) through a low magnification (2x) objective lens (NA = 0.055, Edmund Optics) and collection of the emitted green light (510/84 nm filter, Semrock) with an EMCCD camera (EM-C2, QImaging;

1,004 by 1,002 pixels with 4 by 4 binning), at a rate of 10 frames per second (fps). For 2-photon imaging, a 920 nm femtosecond laser beam (Newport MaiTai DeepSee) was raster-scanned using galvo and resonant scanners (Cambridge 6215H and CRS 8K) and focused at 100 - 300 μm depth below the pial surface using a 16x lens (NA = 0.8, Nikon). Fluorescence from GCaMP6 was collected using a band-pass filter (510/84 nm, Semrock) and a GaAsP photomultiplier tube (Hamamatsu). Single imaging planes were collected at 30 fps (1,154 by 512 pixels, 620 by 380 μm field-of-view) using 20 - 60 mW laser power. Blackout material (Thorlabs) blocked stray light from the visual display entering the collection light path.

Visual stimulation

Visual stimuli were presented on a calibrated 22-inch LCD monitor (Samsung SyncMaster 2233RZ, 1,680-by-1,050 pixels resolution, 60 Hz refresh rate, average luminance 59 cd/m^2). The screen was positioned 20 cm in front of the right eye. The visual field covered 0 - 120 degrees central to peripheral field and ± 40 degrees lower to upper field. Stimuli were 12 degree-wide bars filled with alternating (6 Hz) black and white checkerboard patterns (0.05 cpd spatial frequency; 0 / 100% contrast), moving across the screen in one of the four cardinal directions, at a speed of 6°/s, such that a stimulus traveled across the display for approximately 20 s in the horizontal direction, or 13.4 s in the vertical direction. One experimental session consisted of 10 or 20 'trials', with either one or all of the four bar directions used in every trial. Each trial was interspersed by 'blanks' consisting of a full gray screen (10 / 30 s at 50% luminance). To relate astrocyte responses to the timing of visual stimulation, stimulus presentation was synchronized to image acquisition by using a trigger signal from either the EMCCD camera (1-photon, 10 fps) or the slow-axis galvanometer scan pulses (2-photon, 30 fps), controlled by Presentation software (Neurobehavioral Systems).

Pupil tracking

Pupil size was measured using an infrared eye tracking camera, placed in front of the right eye. Infrared light was focused onto the eye with a far-red LED (735 nm, Thorlabs) and collimated lens (Thorlabs). Data was acquired at 30 fps with a CCD camera (AVT Prosilica GC660; Navitar Zoom 6000 lens) and StreamPix software (Norpix). Images were subsequently analyzed using custom software (MATLAB).

DSP-4 administration and analysis of noradrenaline levels

To deplete noradrenaline levels in the cortex, the neurotoxin DSP-4 (N-(2-chloroethyl)-N-ethyl-2-bromobenzylamine hydrochloride; Sigma) was administered using a single intraperitoneal injection of 75 mg/kg DSP-4 in saline. The dose was titrated to ensure depletion of cortical noradrenaline while not causing signs of discomfort or abnormal behavior in mice. A final session of imaging experiments was performed 72 hours post-injection. Upon completion of imaging, mice were sacrificed, brains removed, and cortical hemispheres collected. Tissue was snap-frozen in liquid N_2 and stored at −80°C until use. Five saline-injected animals were used as controls. High-performance liquid chromatography (HPLC) was used to confirm reduction of cortical noradrenaline levels. On the day of HPLC experiments, samples were rapidly thawed, followed by homogenization in 9 volumes (w/v) ice-cold 200 mM perchloric acid, containing 3 mM cysteine and 0.25 mM EDTA.Na_2 (as described [50]). Homogenization was performed in polypropylene tubes, using a hand-held ultrasonic processor (UP50H, Hielscher). After centrifugation (15,000 x g_{Av} for 10 min), the resulting supernatant was transferred to HPLC vials and 20 μl was injected onto a reversed phase column (Alltima HP C18 AQ, inner diameter 4.6 mm, length 250 mm, particle size 5 μm), equilibrated in running buffer (20 mM acetic acid, 0.25 mM EDTA) [51]. After 1 min, bound analytes were eluted using a linear gradient of methanol (0 - 40% (v/v) in running buffer) with a flow rate of 1 ml/min. Signals were detected fluorimetrically (Waters 2475 multi-wavelength fluorescence detector), using an excitation wavelength of 279 nm and an emission wavelength of 320 nm. Chromatograms were analyzed with Breeze 3.20 software (Waters). Standardization was done against known amounts of external noradrenaline (Sigma). Noradrenaline was typically eluted at ~2.5 ml (against a void volume of 2 ml). In some experiments, 0.05% (v/v) trifluoroacetic acid was added to both solvents, improving the retention of noradrenaline (~2.8 ml), allowing cleaner separation from a faster eluting contaminant.

QUANTIFICATION AND STATISTICAL ANALYSIS

Selection of regions of interest (ROIs)

All imaging data were analyzed in MATLAB (Mathworks) and ImageJ (NIH) [40]. All figures were prepared in Adobe Illustrator CS6 (Adobe).

Analysis of calcium signals from 1-photon and 2-photon images was performed by (1) identifying pixels with significant calcium signals, (2) identifying ROIs within primary visual cortex, (3) summing pixel values within these ROIs, and (4) analyzing the resulting time series. For both 1-photon and 2-photon imaging, pixels showing calcium signals were defined as the 25% brightest pixels identified from the product of the mean and the standard deviation of the raw images computed across time.

For 1-photon imaging, camera images were down-sampled in the x and y dimensions by a factor of 10, yielding images of 25-by-26 pixels, meaning each pixel measured approximately 200-by-200 μm in size. The strongest responsive pixel was identified by computing the 'local' Pearson's correlation coefficient from time series of neighboring pixels and selecting the pixel with the highest correlation to its neighbors. Time series were down-sampled by a factor of 10 before computing the correlation. For 2-photon imaging, ROIs corresponding to individual astrocytes were outlined manually, based on a maximum intensity projection of the acquired time series, which allowed clear cell morphology to be determined. ROIs were identified from the first imaging experiment with visual

stimulation. The same ROIs were used in all experiments with the same animal and the same field of view. Prior to analysis, 2-photon images were registered to correct for x-y motion using TurboReg [41].

Analysis of calcium activity time courses

Calcium activity time courses were extracted from raw images by summing image pixel intensities over each ROI and expressing the result as a fractional change. Specifically, we computed dF/F_0, where baseline fluorescence (F_0) is subtracted from raw fluorescence time series data (F) and the result is divided by F_0. F_0 was set to the 10^{th} percentile of F computed for each time series separately. Calcium activity time courses were smoothed with a zero-lag bidirectional lowpass filter with cutoff frequency of 3 Hz. Responses to locomotor activity and visual stimulation were quantified by comparing the maximum dF/F_0 observed in 8- to 25-s windows prior to, or after, onset of visual stimulation or locomotion. Windows for locomotion and visual stimulation were slid independently to be approximately centered on the response peak. Half-widths at half-maximum response were calculated from a subset of calcium transients with amplitudes greater than 2.5 × s.d. of dF/F_0.

Calculation of response maps

1-photon images were processed at their original frame rate of ~10 Hz, whereas 2-photon images were down-sampled in time by a factor of 3, reducing their frame rate from ~31 Hz to ~10 Hz, prior to event-related averaging. Trial averages, in relation to onset of locomotion or visual stimulation, were generated for 1-photon and 2-photon images, yielding image time series that were used for generating the response maps. Response latency was visualized for every pixel by smoothing the time courses with a Savitzky-Golay filter (3^{rd} order, 7 sampling points wide), calculating the peak response time over a window of –5 to +25 s related to locomotion or stimulus onset - and pseudo-coloring latency using a perceptually uniform lookup table [52].

Analysis of locomotion activity

Locomotion signals from the rotary encoder were resampled at the respective frame rates of the 1-photon or 2-photon imaging stacks. Locomotion events were defined as onsets of movement preceded by a minimum of 8-s during which the animal was stationary. This interval was chosen as it has been shown to be the minimal interval required for consecutive locomotion-induced astrocyte responses of equivalent amplitudes [4]. Locomotion bouts with maximal speeds lower than 5 cm/s and shorter than 1-s duration were discarded from further analyses.

Pupil diameter and arousal state

Pupil dilation was used as a proxy to assess changes in the arousal state of the animals [14, 16], relative to the onset of locomotion or presentation of visual stimuli. For that, the diameter of the pupil was detected in each image using custom code [20] by (1) cropping the image to the eye's margins, (2) smoothing the image using a Gaussian filter, (3) contrast-enhancement using adaptive histogram equalization, (4) binarization resulting in a black-and-white image in which black pixels represent the contours of the pupil, and (5) fitting an ellipsoid to the centermost object - the pupil [20]. Pupil diameter was estimated from the equivalent diameter of the ellipsoid, applying a pixel-to-millimeter conversion assuming an eye size of approx. 3 mm. Parameters for these operations were adjusted manually for each dataset. Resulting pupil diameter time courses were resampled to the frame rates of the 1-photon imaging stacks (~30 Hz to ~10 Hz). Changes in pupil diameter were expressed as changes during 10-s windows after onset of locomotion or visual stimulation, relative to the average diameter in 5-s windows preceding locomotion or stimulation.

Correlation analyses

Pearson's correlation coefficients and their 95% confidence intervals were calculated using a 1,000-fold bootstrap random sampling for the correlations between (1) peak amplitudes and average locomotion speed during visual stimulation, (2) peak amplitudes and pupil diameter changes, and (3) average locomotion speed and pupil diameter changes. Robust linear regression was used to estimate straight-line fits between peak amplitudes and pupil diameter changes, or peak amplitudes and average locomotion speed, respectively.

Statistical analyses

A two-sample Kolmogorov-Smirnov test was used to test the distributions pre- versus post-DSP-4 of (1) peak amplitudes, (2) fraction of locomotion, and (3) frequency of locomotion onsets. A one-way ANOVA was used to compare the means of the distributions pre- versus post-DSP-4 of the bootstrap result for the correlation between peak amplitudes and pupil diameter changes. A two-sample Student's t test was used to compare the means of noradrenaline levels pre- versus post-DSP-4.

DATA AND CODE AVAILABILITY

Analysis code and raw data are available upon request from the corresponding authors Matthew Holt (Matthew.Holt@kuleuven.vib.be) and Vincent Bonin (Vincent.Bonin@nerf.be).